Modeling the Large Deformation and Microstructure Evolution of Nonwoven Polymer Fiber Networks

Mang Zhang
Department of Mechanical Engineering,
State University of New York at Stony Brook,
Stony Brook, NY 11794

Yuli Chen
Institute of Solid Mechanics,
Beihang University (BUAA),
Beijing 100191, China

Fu-pen Chiang
Department of Mechanical Engineering,
State University of New York at Stony Brook,
Stony Brook, NY 11794

Pelagia Irene Gouma
Department of Materials
Science and Engineering,
The Ohio State University,
Columbus, OH 43210

Lifeng Wang[1]
Department of Mechanical Engineering,
State University of New York at Stony Brook,
Stony Brook, NY 11794
e-mail: Lifeng.wang@stonybrook.edu

The electrospinning process enables the fabrication of randomly distributed nonwoven polymer fiber networks with high surface area and high porosity, making them ideal candidates for multifunctional materials. The mechanics of nonwoven networks has been well established for elastic deformations. However, the mechanical properties of the polymer fibrous networks with large deformation are largely unexplored, while understanding their elastic and plastic mechanical properties at different fiber volume fractions, fiber aspect ratio, and constituent material properties is essential in the design of various polymer fibrous networks. In this paper, a representative volume element (RVE) based finite element model with long fibers is developed to emulate the randomly distributed nonwoven fibrous network microstructure, enabling us to systematically investigate the mechanics and large deformation behavior of random nonwoven networks. The results show that the network volume fraction, the fiber aspect ratio, and the fiber curliness have significant influences on the effective stiffness, effective yield strength, and the postyield behavior of the resulting fiber mats under both tension and shear loads. This study reveals the relation between the macroscopic mechanical behavior and the local randomly distributed network microstructure deformation mechanism of the nonwoven fiber network. The model presented here can also be applied to capture the mechanical behavior of other complex nonwoven network systems, like carbon nanotube networks, biological tissues, and artificial engineering networks. [DOI: 10.1115/1.4041677]

Keywords: elastic–plastic materials, large deformation, microstructure evolution, nonwoven networks, layered materials, representative volume element

1 Introduction

Randomly distributed nonwoven fibrous network structures are widely observed in both nature and artificially synthesized materials at different length scales. Naturally existing nonwoven fibrous networks have been well documented, such as silkworm cocoon and extracellular tissues [1,2]. Advances in manufacturing have enabled the fabrication of nonwoven fibrous network with well-defined topologies, for example, paper, carbon nanotubes, proton exchange membrane of fuel cells, and electrospun polymer fiber mats [3–6]. In particular, the electrospinning technique enables us to fabricate randomly distributed nonwoven polymer fibrous networks with high surface area, high porosity, and flexibility, which make them ideal materials for catalysts, filtration, drug delivery, wound dress, and medical textile materials [7–10]. These extensive applications demand a better understanding on the mechanical response of the network and the relation between the network topological factors and the macroscopic mechanical behavior. However, understanding the mechanical properties and deformation mechanisms of the electrospun networks under large deformation is still a challenging task because the macroscopic properties of the distributed nonwoven networks are based on the random microstructure evolution.

Experimental studies on the network microstructure geometry show that the fiber-wrinkled surface topographies, fiber diameters, and fiber orientation arrangement can be controlled by the spinning solution or the spinning processing [11–13]. To simplify the simulation process, fibers in the network can be assumed to have solid circular cross section with same diameter [14,15]. Ideally, randomly distributed nonwoven electrospun fibrous networks can be considered as a two-dimensional (2D) isotropic architecture with porous structures and disordered fiber arrangement [16,17]. The macroscopic deformation mechanisms are determined by the microstructure evolution, which is controlled by the local fiber deformation and the force transition path formation [17,18]. To understand the mechanical response and the underlying deformation mechanisms, extensive studies have been conducted on random nonwoven electrospinning fibrous networks. The experimental researches have shown that the randomly distributed nonwoven electrospinning fibrous network has a good energy-absorption capability, light weight, and similar stiffness with the woven network [19,20]. Moreover, the polypropylene nonwoven fibrous network is also shown to have an excellent stiffness which is notch insensitive [20]. Furthermore, it is shown that the stiffness of nonwoven network is dominated by the material properties and microstructure characteristics including network volume fraction, fiber orientation, and fiber curvature [13,21,22]. Loading rate is another factor that influences the nonwoven network properties, for example, network of Nylon-6,6 (PA66) shows higher stiffness and strength under lower loading rate [23]. Besides these studies on the small deformation, a postyield hardening process is also found broadly in the experimental studies, with a specific ductile behavior and high failure strain exhibited in the randomly distributed nonwoven electrospun network with PLGA (D, L-lattice-co-glycolide), poly(3-hydroxybutyrate-co-4hydroxybutyrate), silk fibroin (SF)/polycaprolactone (PCL), cellulose acetate, and PA66 [24–28].

In parallel to the experimental studies, analytical models and computational frameworks have been developed to understand the deformation mechanism of the random nonwoven fibrous network. Analytical models have reported that the fiber curvature and

[1]Corresponding author.

Contributed by the Applied Mechanics Division of ASME for publication in the Journal of Applied Mechanics. Manuscript received July 11, 2018; final manuscript received October 1, 2018; published online November 2, 2018. Assoc. Editor: Haleh Ardebili.

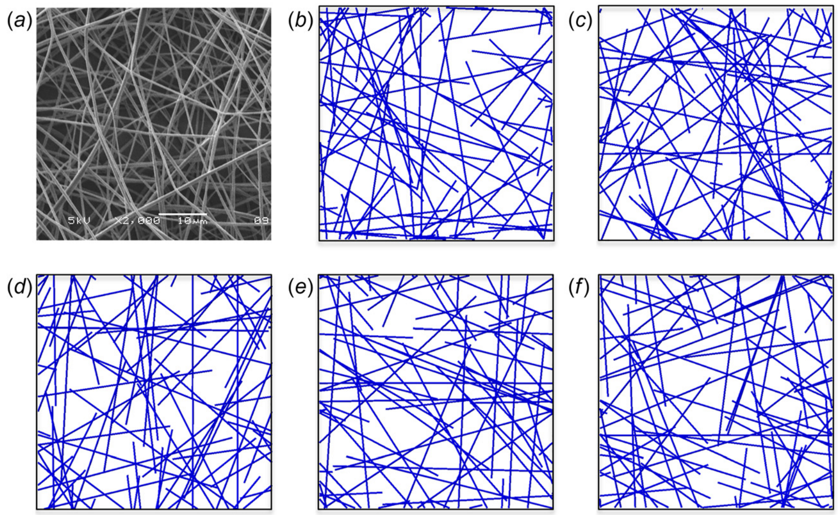

Fig. 1 Randomly distributed nonwoven polymer fiber networks: (*a*) representative SEM image of an electrospun PA6(3)T network (courtesy of Chia-Ling Pai) and (*b*)–(*f*) five RVE models generated with same fibers and geometries but by five different random routines

specimen dimensions can affect the elastic modulus of network but limited in the elastic range [29,30]. Coarse grained molecular dynamics simulation is applied to study the carbon nanotube network, which is also a nonwoven randomly distributed fibrous network. And a postyield hardening process is observed [31,32]. Coarse grained molecular dynamics method can provide results on both microstructure evolution and macro network mechanics, but modeling the electrospun network is still challenging because the size dependence and frictions between fibers are not well considered [33]. Recently, the constitutive model based on the hyperplastic formulation can obtain the macroscopic strain energy density response by adding the contributions of each fiber [34]. A multilayer triangulated network based constitutive model has been developed to study the elastic–plastic behavior of polyamide electrospinning network, with a postyield hardening process consistent with experimental results [35]. Another similar macroscopic model for fiber-reinforced materials with deformable matrices has been derived to capture the progressive alignment of the microconstituents under large deformations [36]. More recently, a constitutive model with the governing equations providing average Cauchy stress, given by volume-averaging theory of a finite size representative volume element (RVE), is built to evaluate the effects of fiber diameter and fiber alignment on the network tensile properties [14,37,38]. These constitutive models have been effective in modeling and understanding the macroscopic mechanical behavior of the randomly distributed nonwoven fibrous network. However, to understand the microstructure evolution and how the microstructure characteristics affect the macroscopic properties, an actual microstructure model is still needed. Since simulating a model with all details has a high computational cost, an RVE is usually applied. Subsequently, the RVE size effect is valued, and the minimum RVE size is found to be related to fiber length, average fiber segment length, fiber diameter, and network volume fraction to represent the whole network behavior [39,40]. A recent study on 2D carbon nanotube nonwoven network in the elastic range has found that the network stiffness is significantly affected by the volume density, leading to the existence of two stiffness thresholds according to whether carbon nanotubes in the network are utilized efficiently to carry load [41,42]. Another novel 2.5D model is recently built to study the mechanics of electrospun networks [43]. In this model, the fiber interaction is only counted when the distance between two fibers is less than a critical distance, which is more accurate. Three-dimensional models are also built to study the short fiber-reinforced network structure [44–47], which is, however, limited in the elastic range with a small deformation (strains within 0.05).

In this study, we develop a long fiber representative volume element model of the randomly distributed nonwoven fibrous networks to investigate the elastic–plastic behavior with large deformation including stiffness, strength, lateral deformation evolution, and the relation between local fiber deformation and the macroscopic deformation behaviors. Various loading conditions such as uniaxial tension, simple shear, and cyclic loading are considered here. Parametric studies are performed to investigate the effects of fiber density, fiber aspect ratio, and fiber curvature on the macroscopic properties of the networks, including the microstructure evolution, elastic deformation, and yield and postyield hardening behaviors.

2 Materials and Methods

2.1 Representative Volume Element. To generate the RVE model, straight fibers with the same length and diameter are initially built with a uniform space distribution in the plane with ABAQUS scripting via Python. Three steps are taken: (1) all fibers are first generated with their middle point on the center of the RVE area; (2) each fiber is then rotated at a random angle from -180 deg to 180 deg; (3) each fiber is transported with a random vector within the boundaries of the RVE area. Obviously, in this way, parts of the fibers fall outside the boundary of the RVE, and those segments of fibers are moved back to the opposite inside. Finally, a network with random fiber orientation and a uniform distribution is generated (see Figs. 1(*b*)–1(*f*)).

In our study, the RVE area is characterized by the dimensions L_1 and L_2, as shown in Fig. 2(*a*). The network architecture is determined by the number of fibers in the RVE area N, the length of a single fiber l, and the fiber diameter d. Considering a single layer network mat, the height of the RVE (network thickness) is same with the fiber diameter under the assumption that fibers are crossed with perfect bonding. The volume fraction or the fiber density of the network can be calculated as the ratio of the fiber volume and the RVE volume

$$f_v = \frac{\pi N l d}{4 L_1 L_2} \tag{1}$$

The fiber aspect ratio is defined as the ratio of the fiber length to the fiber diameter, which is $\lambda = l/d$. Then the network volume fraction can also be given as

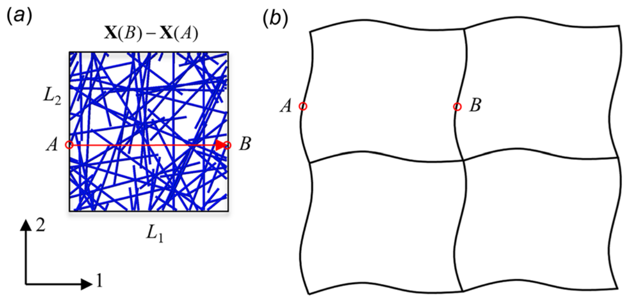

Fig. 2 A spatially periodic RVE: (*a*) the undeformed RVE and (*b*) the deformed RVE with three of its periodic neighbors. The periodic points A and B have reference coordinates X(*A*) and X(*B*).

$$f_v = \frac{\pi N \lambda d^2}{4L_1L_2} \tag{2}$$

For random microstructure materials, the RVE size should be large enough to give statistically homogeneous and ergodic properties [48,49]. The size effect and determination of the minimum model size required to eliminate the size effect of random fiber networks are extensively discussed by Shahsavari and Picu [39]. A critical size, depending on the network density, the fiber length and the fiber bending and axial stiffness, can be used for selection of the size of representative volume elements, above which the predicted mechanical response is model size independent. However, electrospinning process can produce relatively long continuous fibers and the length is determined by the collecting plates with size in the order of ~10 cm [50]. In our simulation, convergence studies are performed (see the Appendix) and the length of nanofibers is not less than the RVE size as indicated by the experiments. Here $d = 1.2\ \mu$m [35], and the selected RVE size $L_1 = L_2 = 0.4$ mm satisfies the minimum model size requirement for homogeneous properties. Rigid connections are considered for the cross links between fibers [17,51]. The RVEs in Fig. 1 shows the networks with $N = 40$, leading to a fiber volume fraction $f_v = 9.42\%$. Five different random network geometries are simulated for each set of network parameters, resulting in an average stress–strain response.

2.2 Materials. The material system in this study is based on the previous experimental work on polyamide PA6 dissolved in dimethylformamide (DMF) with 30 wt% [35]. In our simulations, Young's modulus E_s= 4.1 GPa, Poisson's ratio ν= 0.4, yield stress $\sigma_{ys} = 86$ MPa, postyield slope 760 MPa, and density ρ= 1.14 g/cm^3 are used for the electrospun fibers. Figure 1(*a*) shows a typical randomly distributed nonwoven polymer fiber network.

2.3 Mechanical Loading. The numerical simulations related to the mechanical response of the random nonwoven networks under large deformation are conducted using commercial finite element package ABAQUS/EXPLICIT (Simulia, Provindence, RI). Here we introduce the quasi-static method to discuss the mechanical response of this network under large deformation, with the kinetic energy of the internal energy controlled below 5% to reduce the kinetic effects. And the loading rate is 0.005 mm/s. The strain-controlled periodic boundary conditions (PBCs) are applied to the surface of RVE so that the RVE deforms in a periodically repeating manner without any overlaps or cavities. A principle of virtual work is applied to evaluate the macroscopic network mechanical responses [52,53], which is

$$\delta W^{\text{int}} = \delta W^{\text{ext}} \tag{3}$$

And the external work can be expressed as

$$\delta W^{\text{ext}} = \int_{S_0} \tilde{\mathbf{S}}\mathbf{n}_0 \cdot \delta\mathbf{u}(\mathbf{p})\mathrm{d}S_0 = \int_{S_0} \tilde{\mathbf{s}} \cdot \delta\mathbf{u}(\mathbf{p})\mathrm{d}S_0 \tag{4}$$

where $\tilde{\mathbf{S}}$ is the first Piola–Kirchhoff tensor, $\mathbf{n}_0$ is the normal vector of the surface area, S_0 is the reference configuration, $\delta\mathbf{u}(\mathbf{p})$ is the virtual displacement of point $\mathbf{p}$, and $\tilde{\mathbf{s}}$ is the surface traction. While the internal virtual work can be written as

$$\delta W^{\text{int}} = V_0\mathbf{S} \cdot \delta\mathbf{F} \tag{5}$$

where V_0 is the volume under the reference configuration, $\mathbf{S}$ is the macroscopic first Piola–Kirchhoff stress tensor, and $\mathbf{F}$ is the macroscopic deformation gradient.

To apply the PBCs, considering a periodic repeating point pair A and B locating on left surface and the right surface of RVE, respectively, the constraint on the relative displacement of points A and B is that

$$\mathbf{u}(B) - \mathbf{u}(A) = (F - I)\{\mathbf{X}(B) - \mathbf{X}(A)\} = \mathbf{H}\{\mathbf{X}(B) - \mathbf{X}(A)\} \tag{6}$$

where $\mathbf{u}$ is the displacement, $\mathbf{F}$ is the deformation gradient tensor, $\mathbf{X}$ is the undeformed reference configuration, and $\mathbf{H}$ is the macroscopic displacement gradient tensor. For plane strain problem in this paper, $\mathbf{H}$ can be reduced to a 2 × 2 matrix

$$\mathbf{H} = \begin{bmatrix} H_{11} & H_{12} \\ H_{21} & H_{22} \end{bmatrix} = \begin{bmatrix} F_{11} - 1 & F_{12} \\ F_{21} & F_{22} - 1 \end{bmatrix} \tag{7}$$

In finite element implementation, the components of $\mathbf{H}$ are assigned as the displacement components of the two reference nodes in the RVE. Then, the macroscopic mechanical response of the RVE under various loading conditions can be captured using the principle mentioned earlier. In this paper, the uniaxial tensile loading of overall strain 0.4 is applied as

$$\mathbf{H} = \begin{bmatrix} 0.4 & 0 \\ 0 & H_{22} \end{bmatrix} \tag{8}$$

while the simple shear loading of overall strain 0.4 is applied as

$$\mathbf{H} = \begin{bmatrix} 0 & 0.4 \\ 0 & 0 \end{bmatrix} \tag{9}$$

3 Results and Discussion

3.1 Mechanical Behavior Under Tension. Uniaxial tensile loadings are applied to five different samples, which have same geometry parameters $N = 40$, $l = 0.4$ mm, and $f_v = 9.42\%$. The simulated stress–strain curve and the transverse strain curve are plotted in Fig. 3. The solid line shows the average of five samples, and the red shadow indicates the standard deviation errors of the stress, the transverse strain, and the network porosity $(1 - f_v)$ of those five samples. The yield point is measured from the stress–strain curve by finding the intersection point for the extended line of the linear elastic part and the extended line of the postyield part. The stress on that point is considered as the yield stress, and the strain corresponding to that stress on the stress–strain curve is considered as the yield strain. Postyield hardening slope is measured by the slope of linear hardening part of the stress–strain curve. From the stress–strain curve, the RVE network has an effective Young's modulus E^*= 62.2 MPa, a normalized Young's modulus $E^*/E_s = 0.015$, an effective yield stress σ_y^*= 1.5 MPa, an effective yield strain ε_y^*=0.02, and the average postyield hardening slope of 18 MPa. These overall properties of the nonwoven network agree well with the experimental results [35]. The simulated stress level is slightly lower than the experimental results at the same strain level, which arises from the smaller volume fraction of the network. The volume fraction effect is discussed in Sec. 3.5. From the stress contour in Fig. 3(*d*), the local stress distribution and the microstructure evolution of the network are clearly shown. To give an insight of the

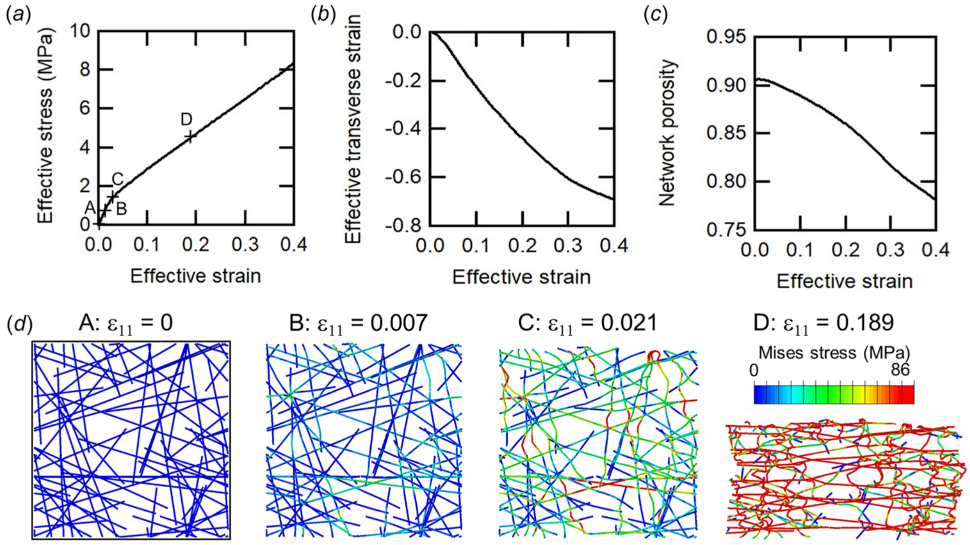

Fig. 3 Mechanical response of the random nonwoven fibrous network under uniaxial tensile loading where $N = 40$ and $l = 0.4$ mm: (*a*) effective stress versus effective strain, (*b*) effective transverse strain versus effective axial strain showing a nonlinear behavior with ratio greater than 1 after 0.05 effective strain, (*c*) average network porosity change during loading, and (*d*) von Mises stress contour for A, B, C, and D points marked in (*a*), respectively

local fiber elastic–plastic behavior, fibers with von Mises stress over the single fiber yield stress (86 MPa) are marked in red. Point A shows the initial condition of the network without any strain. Point B shows the linear elastic stage with the total effective strain of 0.021, where small local deformations can be observed but the network architecture is retained. In this elastic stage, no fibers are observed to yield. Point C is at the yield point where stresses are observed in fibers in the lateral orientation, and fiber bending and buckling start to appear in those fibers. From the contour shown, fiber yielding mostly takes place in the fibers in the lateral orientation under bending. Point D shows the stage in the postyield hardening region. In the hardening process, fiber reorientation causes the microstructure evolution of the network. More fibers yield, and bend or rotate to the elongation direction of tensile loading, leading to a large contraction in the lateral direction. The instantaneous network stiffness is mainly contributed by the fibers in the elongation direction.

From the transverse strain curve in Fig. 3(*b*), the effective Poisson's ratio is small at the beginning of the deformation, where the network here can keep the origin shape and architecture and the reorientations of local fibers have not begun yet. As the overall axial strain increases, contraction in the transverse direction becomes obvious, and the ratio of the transverse strain to axial strain gains, even greater than one due to the rearrangement of fibers in the network microstructure. This rearrangement includes reorientation and bundling of fibers in the network. In this process, fibers along the deformation direction are stretched, while other fibers tend to fold or bend to the elongation direction. As a result, fibers arrange in a denser architecture than the initial one. To further explain the network contraction, network porosity is plotted in Fig. 3(*c*). Here, the total volume of fibers is considered as a constant and the RVE size is reducing during the deformation, which indicates a dramatic decrease of the network porosity. Note that this phenomenon cannot be observed in an isotropic material because anisotropy is introduced in the nonwoven fiber network during the tensile loading, leading to an anisotropic and denser network. These results agree well with both experimental studies and constitutive models [35], but our results highlight the large deformation and the network microstructure evolution.

3.2 Mechanism of Microstructure Evolution. To understand the deformation mechanism of the nonwoven fibrous network, it is instructive to consider the microstructure evolution of the network under uniaxial tension. The deformation of local fibers can be categorized into three types: bending, stretching, and buckling [54]. Among all these three types of local deformation, stretching is the one which can carry the largest load. Consequently, the network with more percentage of stretching deformation has larger stiffness per unit area. Bending can also contribute the macroscopic stiffness to the network mat and will cause the reorientation of fibers and transverse contraction in the network. Buckling is also observed in the microstructure evolution, sometimes combined with bending, and may turn into bending or stretching due to the fiber rearrangement during the deformation. These different types of local fiber deformation are determined by the network microarchitecture.

In the finite element simulation, six typical deformation mechanisms of microstructure evolution according to different fiber connections and fiber orientations under uniaxial tension are captured. For the local structure containing two fibers, two kinds of microstructure evolution are observed: (1) For the first case, both two fibers are aligned in the directions with a considerable angel to the tensile direction (Fig. 4(*a*)), and these fibers will rotate first and then undergo the stretching deformation. (2) For the second case, one fiber lies in the tensile direction and the other fiber is approximately vertical to the tensile direction. It is easy to see that the fiber in the tensile direction tends to be stretched, while the vertical fiber tends to be bent (Fig. 4(*b*)). Furthermore, the vertical fiber may also undergo buckling deformation after a critical strain as the RVE tends to concentrate in the lateral direction. For the three-fiber local structure, it could be more complex, and four kinds of microstructure evolution are observed in the simulation: (1) In the first case, two fibers lie in the tensile direction and the other fiber lies in the direction that has an angle to the tensile direction (Fig. 4(*c*)). As tensile loading applied, the inclined fiber rotates to the tensile direction and then is stretched, while other two fibers are simply extended. (2) In the second case, two fibers are in the tensile direction and the other fiber is approximately vertical to the tensile direction (Fig. 4(*d*)). The vertical fiber undergoes buckling or bending first and then folded, while the network keeps concentrating in the lateral direction. (3) In the third case, three fibers form a triangular frame with one of them vertical to the tensile direction (Fig. 4(*e*)). In this way, the vertical fiber tends to bend or buckle during the deformation, while other

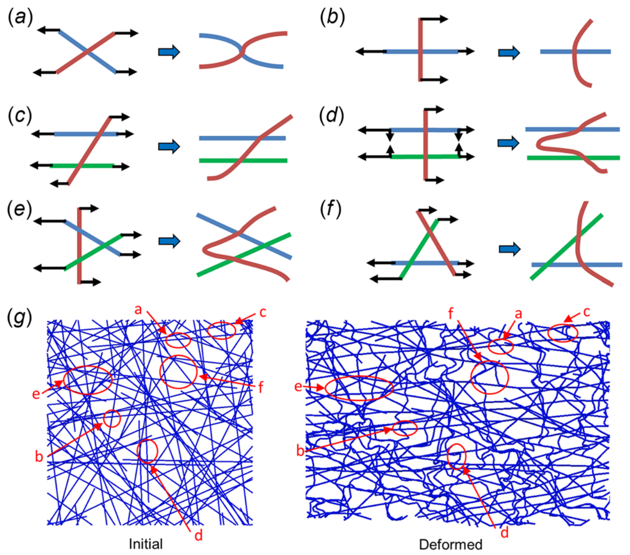

Fig. 4 (*a*)–(*f*) Typical local deformation mechanisms of microstructure evolution in the fibrous network RVE under tensile loading and (*g*) original network microstructure and deformed network microstructure with highlights of six typical deformation mechanisms, where $N = 60$ and $l = 0.6$ mm

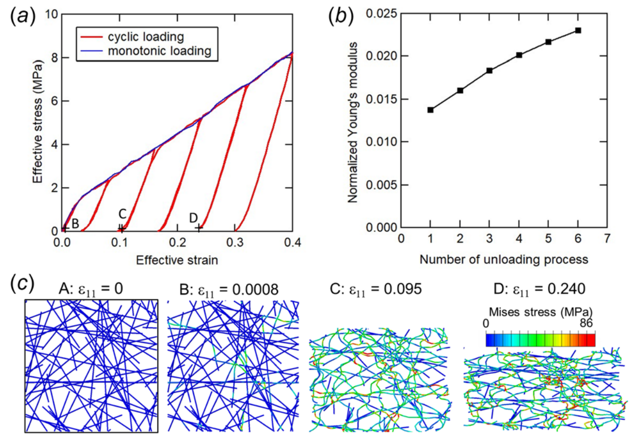

Fig. 5 Mechanical response of the random nonwoven fibrous network under cyclic uniaxial tensile loading ($N = 40$ and $l = 0.4$ mm): (*a*) the stress–strain curve, (*b*) evolution of the normalized Young's modulus for reloading after each uniaxial tensile cycle, and (*c*) von Mises stress contour for the initial network, as well as B, C, and D points marked in (*a*), which are the relaxed networks after the first, third, and fifth cycles, respectively

two fibers tend to bend and then stretch. (4) In the last case, three fibers form a triangular frame with one of them aligned to the tensile direction (Fig. 4(*f*)). Here, fibers in the direction close to the tensile direction are stretched and other fibers undergone rotation, bending, buckling, or folding, which can be expanded to other polygons built by more fibers. All these local microstructure deformations can be found in the simulation results in Fig. 4(*g*) highlighted by red circles.

3.3 Mechanical Behavior Under Cyclic Loading. After studies on the mechanical response of the randomly distributed nonwoven fibrous networks under monotonic tensile loading, simulations under cyclic tensile loading are also performed to investigate the deformation mechanisms under loading, unloading, and reloading cycles. Since the loading rate is small for quasi-static

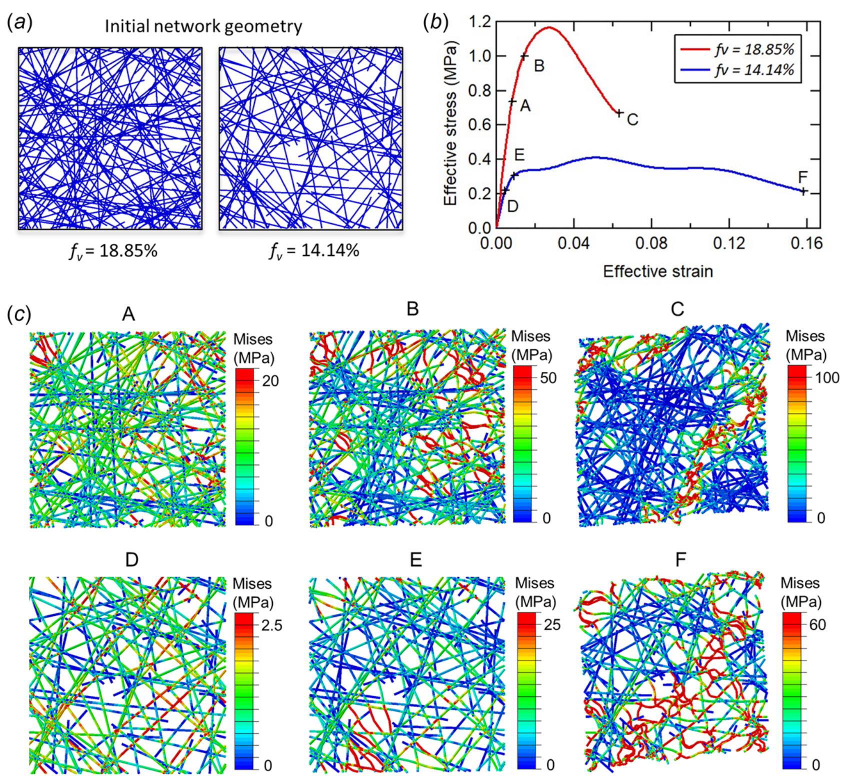

Fig. 6 Mechanical response of the random nonwoven fibrous network under simple shear loading ($l = 0.5$ mm, $N = 72$ and 48): (*a*) the initial network geometry for RVEs with $f_v = 18.85\%$ and $f_v = 14.14\%$, (*b*) the shear stress–strain response of the two RVEs under simple shear, and (*c*) the corresponding deformed configurations with von Mises stress distribution at different levels of shear strain

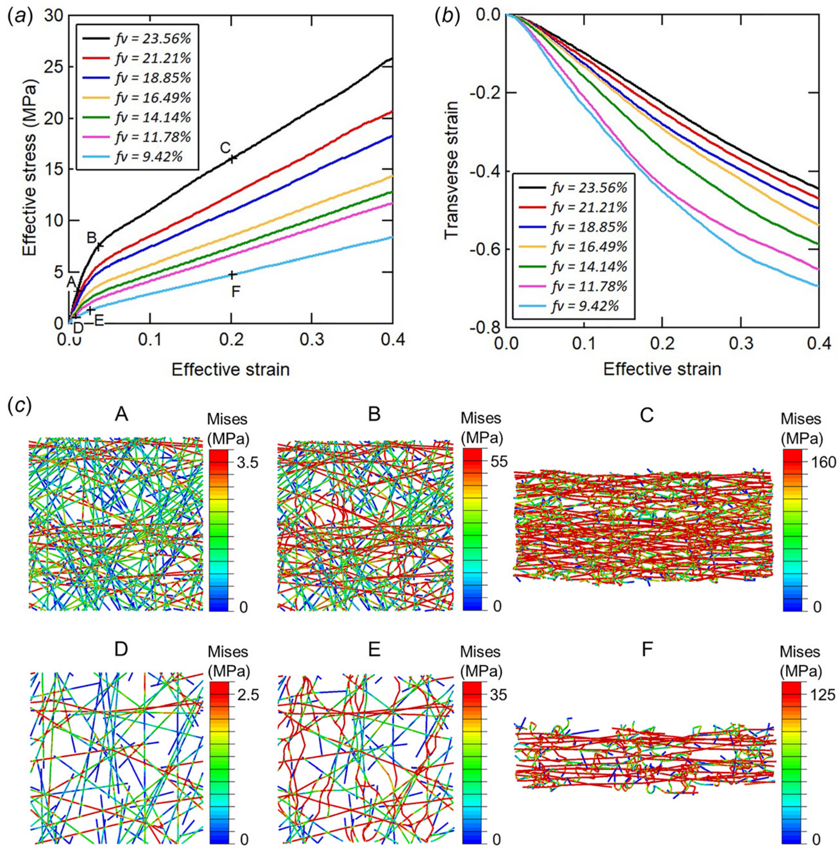

Fig. 7 Mechanical response of random nonwoven fibrous networks with different volume fractions under uniaxial tensile loading (f_v varies from 9.42% to 23.56%): (*a*) effect of volume fraction on the stress–strain curves, (*b*) effect of volume fraction on the transverse strain, and (*c*) the corresponding microstructures and von Mises stress distribution for six points marked in (*a*)

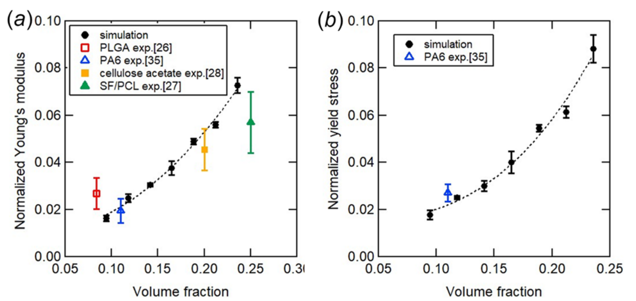

Fig. 8 (*a*) Normalized Young's modulus of networks with different fiber volume fractions of present simulation and other experimental results [26–28,35] and (*b*) the normalized yield stress of networks with different fiber volume fractions

method, viscoelastic is not considered here. The stress–strain response for six loading cycles is plotted in Fig. 5(*a*), where the unloading and reloading responses follow the same trace on the stress–strain curve. The reloading curve follows the same trace as the unloading one. In the elastic stage, both unloading and reloading curves show linear behavior. While in the hardening region, when the overall stress is close to zero, the unloading and reloading curves show small rollover and the reloading hysteresis. During the unloading process, some fibers with permanent plastic deformations undergo compression, leading to the rotation at the intersections between fibers. While at the beginning of reloading process, releasing of compression and rotation causes the hysteresis shown on a curve.

Besides the comparison with monotonic loading, the effective stiffness of the network is observed to increase during the cyclic loading process. To highlight the stiffness enhancement, Young's modulus is measured for each reloading curve. As shown in Fig. 5(*b*), the normalized Young's modulus increases as the unloading–reloading cycle is applied, with the normalized Young's modulus increased from 0.014 to 0.023 after six loading cycles. This stiffness enhancement has also been captured in the experimental study [35]. The increasing Young's modulus is mainly due to the microstructure evolution and the local plastic deformation of the fibers during loading/unloading [55]. Figure 5(*c*) shows the residual stress in fibers and the deformed network microstructures at a different level of residual overall strains after unloading. Higher residual stress is seen with higher loading strain due to the hardening effect in each fiber. Also, most fibers in the network are realigned toward to the loading condition after each loading cycle, leading to more fibers contributing to load carrying in the tensile direction. Furthermore, the cross-sectional area of the network is decreased significantly. All these directly result in the enhancement of the overall stiffness of the network.

3.4 Mechanical Behavior Under Shear. The randomly distributed nonwoven fibrous network under simple shear is also investigated with two different network volume fractions. Both RVE models have the same fiber length of $l = 0.5$ mm and fiber diameter $d = 1.2$ μm, but a different number of fibers $N = 72$ and 48, leading to the volume fraction $f_v =$ 18.85% and 14.14%, respectively. The initial network geometry of these two RVEs is shown in Fig. 6(*a*).

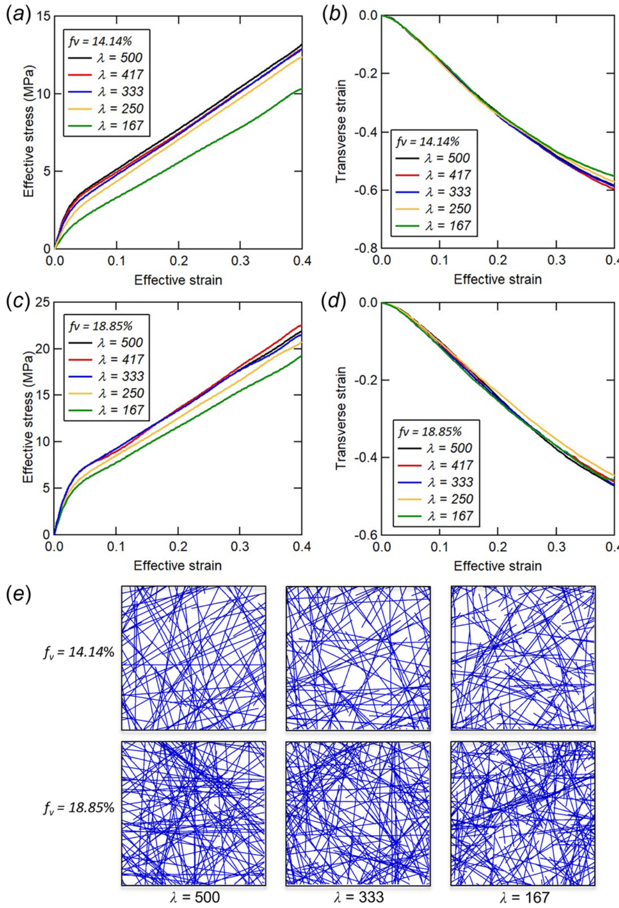

Fig. 9 Mechanical response of random nonwoven fibrous networks with different fiber aspect ratios under uniaxial tensile loading ($f_v = 14.14\%$ and 18.85%): (*a*) effect of fiber aspect ratio on the stress–strain curves for $f_v = 14.14\%$, (*b*) effect of fiber aspect ratio on the transverse strain for $f_v = 14.14\%$, (*c*) effect of fiber aspect ratio on the stress–strain curves for $f_v = 18.85\%$, (*d*) effect of fiber aspect ratio on the transverse strain for $f_v = 18.85\%$, and (*e*) and (*f*) the initial network microstructure for fiber aspect ratio $\lambda = 500$, 333, and 167, while $f_v = 14.14\%$ and 18.85%, respectively

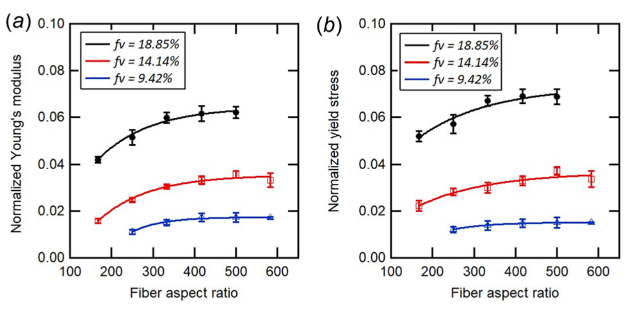

Fig. 10 (*a*) Normalized Young's modulus of the network as a function of fiber aspect ratio and (*b*) normalized yield stress of the network as a function of fiber aspect ratio

Table 1 The values of coefficients A_1, A_2, and A_3 at different volume fractions f_v

f_v	A_1	A_2	A_3
18.85%	0.064	−0.812	0.008
14.14%	0.035	−0.791	0.008
9.42%	0.017	−0.203	0.013

Figure 6(*b*) depicts the overall stress–strain response of the two RVEs under simple shear loading. As expected, the network with higher volume fraction has a higher overall shear modulus of $G = 98$ MPa, as compared to 54 MPa for the network with lower volume fraction. Figure 6(*c*) shows the corresponding deformed configurations with von Mises stress distribution at different levels of shear strain marked in Fig. 6(*b*). In the linear elastic region, for cases A and D, stresses are observed in fibers in diagonal directions because of the global shear deformation. When the network starts to yield, for cases B and E, fibers in 135 deg direction starts to bend and buckle. These fibers start to fold and collapse as the strain increases. For cases C and F, shear bands are formed globally due to the collapses of local fibers, indicating significant local deformation as compared to the case under tensile loading. This also leads to the stress drop in the shear stress–strain response, especially for the network with larger volume fraction. These results provide interesting structure–property relationships for the nonwoven fibrous network.

3.5 Effect of Fiber Volume Fraction.

Figure 7 presents the mechanical response of random nonwoven fibrous networks with different volume fractions under uniaxial tensile loading. Here $l = 0.4$ mm, $d = 1.2\ \mu$m, and f_v vary from 9.42% to 23.56% (N from 40 to 100). The strain–stress curves of these networks under uniaxial tension are shown in Fig. 7(*a*). As expected, networks with higher volume fraction are stiffer and stronger than the networks with lower volume fraction. The volume fraction also influences the lateral contraction during tension. Due to the lower cross links density in the networks with lower volume fraction, the fibers inside have a higher degree of freedoms to bend and rotate, which makes these networks contract much more in the lateral direction, as shown in Fig. 7(*b*). Clearly, larger volume fraction can reduce the densification effect during the tensile loading. This is also verified by the deformed configuration shown in Fig. 7(*c*). In this study, for cases *C* and *F*, the deformed networks are at the macroscopic strain of 0.2, but the network with $f_v = 9.42\%$ has a much smaller height, which is almost 50% of the height of the network with $f_v = 23.56\%$.

To further understand the effects of fiber volume fraction on the network properties, effective Young's modulus E^* and yield stress σ_y^* are calculated from the stress–strain curves. The Young's modulus is normalized by the fiber modulus E^*/E_s in Fig. 8(*a*). The normalized Young's modulus increases from 0.015 to 0.073 as f_v increases from 9.42% to 23.56%. The relationship between normalized Young's modulus and volume fraction can be expressed as

$$E^*/E_s = C(f_v)^n \tag{10}$$

where coefficient $C = 0.653$ and $n = 1.557$. The networks discussed earlier can be considered as bending dominated structures with $n > 1.5$ [56,57]. This bending dominated feature is consistent with the contour shown in Fig. 7(*c*). The prediction is able to precisely capture the experimental results of different volume fraction and material [26–28,35]. At larger volume fractions, the results show slightly higher values, which could arise from the perfect fiber bonding assumption. Yield stress for the network is normalized with fiber yield stress, which increases from 0.018 to 0.088 as f_v increases from 9.42% to 23.56%. The relationship between normalized yield stress and volume fraction can also be expressed as

$$\sigma_y^*/\sigma_y^s = D(f_v)^m \tag{11}$$

with $D = 0.890$ and $m = 1.638$, as shown in Fig. 8(*b*).

3.6 Effect of Fiber Aspect Ratio.

Besides the effect of the volume fraction of the randomly distributed nonwoven fibrous network, another important parameter that can affect the mechanical response is the fiber aspect ratio. To understand this effect, networks with $\lambda = 167$ to $\lambda = 583$ (fixed $d = 1.2\ \mu$m) are considered on networks with $f_v = 9.42\%$, 14.14%, and 18.85%, respectively. The stress–strain curves are plotted in Figs. 9(*a*) and 9(*c*), which clearly indicate that higher fiber aspect ratio leads to higher stiffness and yield stress for the networks. However, the fiber aspect ratio has little effect on the lateral contraction as seen in the transvers strain in Figs. 9(*b*) and 9(*d*). This is because in our model, only long fibers are considered in the network due to the electrospinning process, where each fiber has many cross links with others. On the contrary, fiber aspect ratio can significantly affect the transverse strain for short fiber networks. This is also true for the effective stiffness and yield stress, as seen in Fig. 9(*a*). When the fibers are long enough, the aspect ratio has little effect on the stress–strain response. This suggests that, at each volume fraction, a critical fiber aspect ratio exists, beyond which the mechanical response of the network is not sensitive to the fiber aspect ratio. On the other hand, current model is capable to simulate the mechanical behaviors of the network with intermediate fiber aspect ratio, providing a more general solution.

To quantitatively show the effect of fiber aspect ratio on the macroscopic network mechanical behaviors, normalized Young's modulus and yield stress are calculated and plotted in Fig. 10. The relation between λ and the normalized Young's modulus can be described by

$$E^*/E_s = A_1 - A_2 e^{-A_3 \cdot \lambda} \tag{12}$$

where coefficients A_1,A_2, and A_3 can be obtained by fitting the curve, and their values are listed in Table 1. As λ goes to infinite, A_1 represents the maximum value the network can achieve at the a given fiber volume fraction. It is interesting that the network with higher f_v tends to reach the A_1 at a lower λ, which is due to more crosslinks and smaller average fiber segment length. Therefore, the nonwoven fiber networks with fibers of infinite length can be simplified to the networks with fibers of large aspect ratio. Similar correlation is also observed for the network yield stress versus fiber aspect ratio. For the network with $f_v = 14.14\%$, as fiber aspect ratio λ increases from 167 to 500, the normalized yield stress increases from 0.022 to 0.037. While for the network with $f_v = 18.85\%$, as fiber aspect ratio λ increases from 167 to 500, the normalized yield stress increases from 0.052 to 0.069. These results suggest how the randomly distributed nonwoven network can efficiently carry the load by optimizing the fiber aspect ratio.

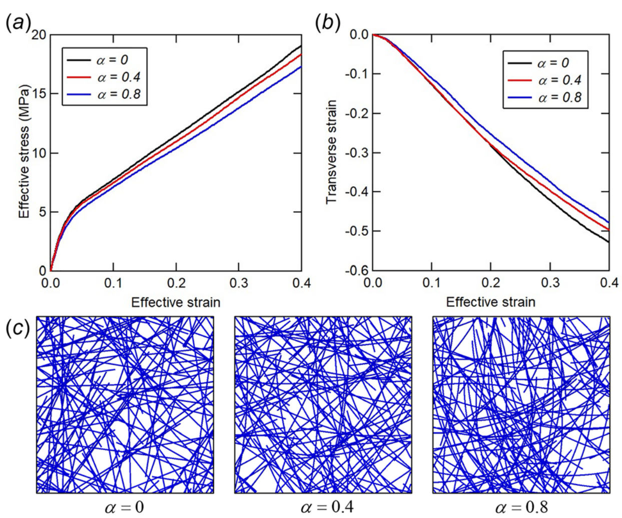

Fig. 11 Mechanical response of random nonwoven fibrous networks with different fiber aspect ratios under uniaxial tensile loading: (*a*) the stress–strain curves with fiber radians of 0, 0.4, and 0.8, (*b*) the effective transverse strain, and (*c*) the schematic diagram of fibrous networks with different fiber radian α

3.7 Effect of Fiber Curvature. Fibers in the network are easy to be curved during the electrospinning process (see Fig. 1(*a*)) due to the large aspect ratio. The curliness of fibers may degrade the mechanical properties of the network. Therefore, the influence of the fiber curliness on the network stiffness and strength is also studied here. To simplify the problem, the network is modeled with fibers of the same length l and same curvature radius R, then the radian of the arc can be expressed as $\alpha = l/R$. Figure 11 presents three networks with same volume fraction ($f_v = 18.85\%$) and fiber length ($l = 0.4$ mm), but different fiber radians ($\alpha = 0$, 0.4, and 0.8). When $\alpha = 0$, fibers are straight, same as the model shown in Fig. 1(*c*), and the Young's modulus of 206 MPa and the yield stress of 4.4 MPa are observed. As α increases to 0.8, the network has a Young's modulus (178 MPa) and yield stress (3.8 MPa), which are slightly smaller than those of the network with straight fibers (Fig. 11(*a*)). These results indicate that the simulation model with straight fibers is applicable to the networks with slightly curved fibers.

4 Conclusion

In summary, we have studied the mechanical response of electrospun nonwoven fibrous networks under large deformation with elastic–plastic fibers. The elastic and plastic properties of the networks under uniaxial tensile loading, cyclic loading, and simple shear loading are investigated, and the relation between macroscopic properties and the microstructure evolution is revealed. It is shown that the network volume fraction, the fiber aspect ratio, and the fiber curliness have important influences on the network stiffness and strength. Our modeling provides a solid theoretical foundation for the design, optimization, and property prediction of randomly distributed nonwoven fibrous networks. This method has a limitation to identify the fiber-to-fiber interaction properties in the networks, where rigid perfect bonding is assumed. Future work will include the fiber-to-fiber interaction as well as network fractures in the model to expand deep understanding of the mechanics of randomly distributed nonwoven fibrous networks.

Acknowledgment

L. Wang acknowledges the Office of Naval Research (Dr. Yapa Rajapakse, Solid Mechanics Program). The authors are also grateful to Dr. Chia-Ling Pai and Dr. Yanyu Chen for valuable discussions.

Funding Data

- The National Science Foundation (Grant No. CMMI-1724342).

Appendix: Effects of Size and Boundary Conditions of Representative Volume Element

The size effect and convergence of the simulation results are investigated in this study. The simulated Young's modulus of the random nonwoven fibrous networks is shown in Fig. 12 with three different RVE sizes. It can be observed that no significant size effect is found on the calculated Young's modulus. Reducing RVE size from 1.2 mm to 0.4 mm only leads to slightly changes in the Young's modulus. Optimally, $L_1 = L_2 = 0.4$ mm is acceptable to provide minimum model size to give statistically homogeneous and ergodic properties in this work.

On these RVEs, the boundary conditions can affect the simulation results either. Periodic boundary conditions are often chosen for approximating a large system by using a small part or a unit cell. Homogeneous displacement BCs are usually over-constraint compared with periodic PBCs. We have compared the results of same RVEs with PBCs and homogeneous displacement BCs, respectively. In Fig. 12, clearly the difference of the results of RVEs two types of BCs is negligible, considering that the errors

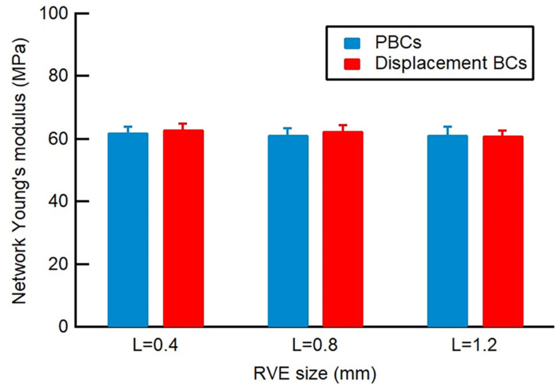

Fig. 12 The RVE size effect and boundary condition effect on the network Young's modulus

caused by the randomness of the fiber network are larger. This indicates that the RVEs with PBCs in our simulation are appropriate and able to reduce the boundary effects.

References

[1] Chen, F. J., Porter, D., and Vollrath, F., 2012, "Morphology and Structure of Silkworm Cocoons," Mat. Sci. Eng. C-Mater., **32**(4), pp. 772–778.
[2] Camelliti, P., Borg, T. K., and Kohl, P., 2005, "Structural and Functional Characterisation of Cardiac Fibroblasts," Cardiovasc. Res., **65**(1), pp. 40–51.
[3] Snow, E. S., Novak, J. P., Campbell, P. M., and Park, D., 2003, "Random Networks of Carbon Nanotubes as an Electronic Material," Appl. Phys. Lett., **82**(13), pp. 2145–2147.
[4] El-Kharouf, A., Mason, T. J., Brett, D. J. L., and Pollet, B. G., 2012, "Ex-Situ Characterisation of Gas Diffusion Layers for Proton Exchange Membrane Fuel Cells," J. Power Sources, **218**, pp. 393–404.
[5] Henriksson, M., Berglund, L. A., Isaksson, P., Lindstrom, T., and Nishino, T., 2008, "Cellulose Nanopaper Structures of High Toughness," Biomacromolecules, **9**(6), pp. 1579–1585.
[6] Li, D., and Xia, Y. N., 2004, "Electrospinning of Nanofibers: Reinventing the Wheel?," Adv. Mater., **16**(14), pp. 1151–1170.
[7] Khil, M. S., Cha, D. I., Kim, H. Y., Kim, I. S., and Bhattarai, N., 2003, "Electrospun Nanofibrous Polyurethane Membrane as Wound Dressing," J. Biomed. Mater. Res. Part B: Appl. Biomater., **67**(2), pp. 675–679.
[8] Gopal, R., Kaur, S., Ma, Z., Chan, C., Ramakrishna, S., and Matsuura, T., 2006, "Electrospun Nanofibrous Filtration Membrane," J. Membr. Sci., **281**(1–2), pp. 581–586.
[9] Zamani, M., Prabhakaran, M. P., and Ramakrishna, S., 2013, "Advances in Drug Delivery Via Electrospun and Electrosprayed Nanomaterials," Int. J. Nanomed., **8**, p. 2997.
[10] Dai, Y., Liu, W., Formo, E., Sun, Y., and Xia, Y., 2011, "Ceramic Nanofibers Fabricated by Electrospinning and Their Applications in Catalysis, Environmental Science, and Energy Technology," Polym. Adv. Technol., **22**(3), pp. 326–338.
[11] Pai, C. L., Boyce, M. C., and Rutledge, G. C., 2011, "On the Importance of Fiber Curvature to the Elastic Moduli of Electrospun Nonwoven Fiber Meshes," Polymer, **52**(26), pp. 6126–6133.
[12] Wang, L., Pai, C.-L., Boyce, M. C., and Rutledge, G. C., 2009, "Wrinkled Surface Topographies of Electrospun Polymer Fibers," Appl. Phys. Lett., **94**(15), p. 151916.
[13] Huang, Z.-M., Zhang, Y.-Z., Kotaki, M., and Ramakrishna, S., 2003, "A Review on Polymer Nanofibers by Electrospinning and Their Applications in Nanocomposites," Compos. Sci. Technol., **63**(15), pp. 2223–2253.
[14] Stylianopoulos, T., Bashur, C. A., Goldstein, A. S., Guelcher, S. A., and Barocas, V. H., 2008, "Computational Predictions of the Tensile Properties of Electrospun Fibre Meshes: Effect of Fibre Diameter and Fibre Orientation," J. Mech. Behav. Biomed. Mater., **1**(4), pp. 326–335.
[15] Nasouri, K., Bahrambeygi, H., Rabbi, A., Shoushtari, A. M., and Kaflou, A., 2012, "Modeling and Optimization of Electrospun PAN Nanofiber Diameter Using Response Surface Methodology and Artificial Neural Networks," J. Appl. Polym. Sci., **126**(1), pp. 127–135.
[16] Rodney, D., Gadot, B., Martinez, O. R., du Roscoat, S. R., and Orgeas, L., 2016, "Reversible Dilatancy in Entangled Single-Wire Materials," Nat. Mater., **15**(1), pp. 72–77.
[17] Picu, R. C., 2011, "Mechanics of Random Fiber Networks: A Review," Soft Matter, **7**(15), pp. 6768–6785.
[18] Chaudhuri, O., Parekh, S. H., and Fletcher, D. A., 2007, "Reversible Stress Softening of Actin Networks," Nature, **445**(7125), pp. 295–298.
[19] Ridruejo, A., González, C., and LLorca, J., 2011, "Micromechanisms of Deformation and Fracture of Polypropylene Nonwoven Fabrics," Int. J. Solids Struct., **48**(1), pp. 153–162.
[20] Chen, Y., Ridruejo, A., González, C., Llorca, J., and Siegmund, T., 2016, "Notch Effect in Failure of Fiberglass Non-Woven Materials," Int. J. Solids Struct., **96**, pp. 254–264.
[21] Ceretti, E., Ginestra, P. S., Ghazinejad, M., Fiorentino, A., and Madou, M., 2017, "Electrospinning and Characterization of Polymer–Graphene Powder Scaffolds," CIRP Ann., **66**(1), pp. 233–236.
[22] Choi, W., Lee, S., Kim, S. H., and Jang, J. H., 2016, "Polydopamine Inter-Fiber Networks: New Strategy for Producing Rigid, Sticky, 3D Fluffy Electrospun Fibrous Polycaprolactone Sponges," Macromol. Biosci., **16**(6), pp. 824–835.
[23] Zussman, E., Burman, M., Yarin, A., Khalfin, R., and Cohen, Y., 2006, "Tensile Deformation of Electrospun Nylon-6, 6 Nanofibers," J. Polym. Sci. Part B: Polym. Phys., **44**(10), pp. 1482–1489.
[24] Maksimcuka, J., Obata, A., Sampson, W. W., Blanc, R., Gao, C., Withers, P. J., Tsigkou, O., Kasuga, T., Lee, P. D., and Poologasundarampillai, G., 2017, "X-Ray Tomographic Imaging of Tensile Deformation Modes of Electrospun Biodegradable Polyester Fibres," Front. Mater., **4**, p.43.
[25] Zhang, X., and Chase, G. G., 2016, "Electrospun Elastic Acrylonitrile Butadiene Copolymer Fibers," Polymer, **97**, pp. 440–448.
[26] Li, W. J., Laurencin, C. T., Caterson, E. J., Tuan, R. S., and Ko, F. K., 2002, "Electrospun Nanofibrous Structure: A Novel Scaffold for Tissue Engineering," J. Biomed. Mater. Res. Part A, **60**(4), pp. 613–621.
[27] Yin, Y., Pan, Z., and Xiong, J., 2018, "A Tensile Constitutive Relationship and a Finite Element Model of Electrospun Nanofibrous Mats," Nanomaterials, **8**(1), p. 29.
[28] Stylianopoulos, T., Kokonou, M., Michael, S., Tryfonos, A., Rebholz, C., Odysseos, A. D., and Doumanidis, C., 2012, "Tensile Mechanical Properties and Hydraulic Permeabilities of Electrospun Cellulose Acetate Fiber Meshes," J. Biomed. Mater. Res. Part B: Appl. Biomater., **100**(8), pp. 2222–2230.
[29] Kumar, V., and Rawal, A., 2017, "Elastic Moduli of Electrospun Mats: Importance of Fiber Curvature and Specimen Dimensions," J. Mech. Behav. Biomed. Mater., **72**, pp. 6–13.
[30] Ban, E., Barocas, V. H., Shephard, M. S., and Picu, C. R., 2016, "Effect of Fiber Crimp on the Elasticity of Random Fiber Networks With and Without Embedding Matrices," ASME J. Appl. Mech., **83**(4), p. 041008.
[31] Wang, C., Wang, L. F., and Xu, Z. P., 2013, "Enhanced Mechanical Properties of Carbon Nanotube Networks by Mobile and Discrete Binders," Carbon, **64**, pp. 237–244.
[32] Wang, C., Xie, B., Liu, Y. L., and Xu, Z. P., 2012, "Mechanotunable Microstructures of Carbon Nanotube Networks," Acs Macro. Lett., **1**(10), pp. 1176–1179.
[33] Wei, X., Xia, Z., Wong, S.-C., and Baji, A., 2009, "Modelling of Mechanical Properties of Electrospun Nanofibre Network," Int. J. Exp. Comput. Biomech., **1**(1), pp. 45–57.
[34] Gasser, T. C., Ogden, R. W., and Holzapfel, G. A., 2006, "Hyperelastic Modelling of Arterial Layers With Distributed Collagen Fibre Orientations," J. R. Soc., Interface, **3**(6), pp. 15–35.
[35] Silberstein, M. N., Pai, C. L., Rutledge, G. C., and Boyce, M. C., 2012, "Elastic-Plastic Behavior of Non-Woven Fibrous Mats," J. Mech. Phys. Solids, **60**(2), pp. 295–318.
[36] Planas, J., Guinea, G., and Elices, M., 2007, "Constitutive Model for Fiber-Reinforced Materials With Deformable Matrices," Phys. Rev. E, **76**(Pt 1), p. 041903.
[37] Stylianopoulos, T., and Barocas, V. H., 2007, "Volume-Averaging Theory for the Study of the Mechanics of Collagen Networks," Comput. Methods Appl. Mech. Eng., **196**(31–32), pp. 2981–2990.
[38] Stylianopoulos, T., and Barocas, V. H., 2007, "Multiscale, Structure-Based Modeling for the Elastic Mechanical Behavior of Arterial Walls," ASME J. Biomech. Eng., **129**(4), pp. 611–618.
[39] Shahsavari, A. S., and Picu, R. C., 2013, "Size Effect on Mechanical Behavior of Random Fiber Networks," Int. J. Solids Struct., **50**(20–21), pp. 3332–3338.
[40] Berkache, K., Deogekar, S., Goda, I., Picu, R., and Ganghoffer, J.-F., 2017, "Construction of Second Gradient Continuum Models for Random Fibrous Networks and Analysis of Size Effects," Compos. Struct., **181**, pp. 347–357.
[41] Pan, F., Chen, Y. L., and Qin, Q. H., 2016, "Stiffness Thresholds of Buckypapers Under Arbitrary Loads," Mech. Mater., **96**, pp. 151–168.
[42] Chen, Y. L., Pan, F., Guo, Z. Y., Liu, B., and Zhang, J. Y., 2015, "Stiffness Threshold of Randomly Distributed Carbon Nanotube Networks," J. Mech. Phys. Solids, **84**, pp. 395–423.
[43] Zündel, M., Mazza, E., and Ehret, A. E., 2017, "A 2.5 D Approach to the Mechanics of Electrospun Fibre Mats," Soft Matter, **13**(37), pp. 6407–6421.
[44] Lu, Z. X., Yuan, Z. S., and Liu, Q., 2014, "3D Numerical Simulation for the Elastic Properties of Random Fiber Composites With a Wide Range of Fiber Aspect Ratios," Comput. Mater. Sci., **90**, pp. 123–129.
[45] Zhang, Y., Lu, Z., Yang, Z., Zhang, D., Shi, J., Yuan, Z., and Liu, Q., 2017, "Compression Behaviors of Carbon-Bonded Carbon Fiber Composites: Experimental and Numerical Investigations," Carbon, **116**, pp. 398–408.
[46] Islam, M., Tudryn, G. J., and Picu, C. R., 2016, "Microstructure Modeling of Random Composites With Cylindrical Inclusions Having High Volume Fraction and Broad Aspect Ratio Distribution," Comput. Mater. Sci., **125**, pp. 309–318.
[47] Islam, M., and Picu, R., 2018, "Effect of Network Architecture on the Mechanical Behavior of Random Fiber Networks," ASME J. Appl. Mech., **85**(8), p. 081011.
[48] Ostoja-Starzewski, M., 2007, *Microstructural Randomness and Scaling in Mechanics of Materials*, Chapman and Hall/CRC, Boca Raton, FL.
[49] Ostoja-Starzewski, M., 2005, "Scale Effects in Plasticity of Random Media: Status and Challenges," Int. J. Plasticity, **21**(6), pp. 1119–1160.
[50] Beachley, V., and Wen, X., 2009, "Effect of Electrospinning Parameters on the Nanofiber Diameter and Length," Mater. Sci. Eng.: C, **29**(3), pp. 663–668.
[51] Deogekar, S., and Picu, R., 2018, "On the Strength of Random Fiber Networks," J. Mech. Phys. Solids, **116**, pp. 1–16.

[52] Wang, L. F., Boyce, M. C., Wen, C. Y., and Thomas, E. L., 2009, "Plastic Dissipation Mechanisms in Periodic Microframe-Structured Polymers," Adv. Funct. Mater., **19**(9), pp. 1343–1350.
[53] Danielsson, M., Parks, D. M., and Boyce, M. C., 2007, "Micromechanics, Macromechanics and Constitutive Modeling of the Elasto-Viscoplastic Deformation of Rubber-Toughened Glassy Polymers," J. Mech. Phys. Solids, **55**(3), pp. 533–561.
[54] Head, D. A., Levine, A. J., and MacKintosh, F. C., 2003, "Distinct Regimes of Elastic Response and Deformation Modes of Cross-Linked Cytoskeletal and Semiflexible Polymer Networks," Phys. Rev. E, **68**(6), p. 061907.
[55] van Oosten, A. S. G., Vahabi, M., Licup, A. J., Sharma, A., Galie, P. A., MacKintosh, F. C., and Janmey, P. A., 2016, "Uncoupling Shear and Uniaxial Elastic Moduli of Semiflexible Biopolymer Networks: Compression-Softening and Stretch-Stiffening," Sci. Rep., **6**, p. 19270.
[56] Buxton, G. A., and Clarke, N., 2007, "'Bending to Stretching' Transition Disordered Networks," Phys. Rev. Lett., **98**(23), p. 238103.
[57] Onck, P., Koeman, T., Van Dillen, T., and van der Giessen, E., 2005, "Alternative Explanation of Stiffening in Cross-Linked Semiflexible Networks," Phys. Rev. Lett., **95**(17), p. 178102.